Title

Topological chaos in active nematics

Permalink

https://escholarship.org/uc/item/17x4g3dq

Journal

Nature Physics, 15(10)

ISSN

1745-2473

Authors

Tan, Amanda J
Roberts, Eric
Smith, Spencer A
et al.

Publication Date

2019-10-01

DOI

10.1038/s41567-019-0600-y

Peer reviewed

Topological chaos in active nematics

Amanda J. Tan,[1] Eric Roberts,[2] Spencer A. Smith,[3] Ulyses Alverado Olvera,[1]
Jorge Arteaga,[1] Sam Fortini,[1] Kevin A. Mitchell,[1] and Linda S. Hirst[1]
[1]*Physics Department, University of California, Merced, CA 95344, USA*
[2]*Applied Math Department, University of California, Merced, CA 95344, USA*
[3]*Department of Physics, Mount Holyoke College, MA 01075, USA*
(Dated: July 13, 2019)

Active nematics are out-of-equilibrium fluids composed of rod-like subunits, which can generate large-scale, self-driven flows. We examine a microtubule-kinesin-based active nematic confined to two-dimensions, exhibiting chaotic flows with moving topological defects. Applying tools from chaos theory, we investigate self-driven advection and mixing on different length scales. Local fluid stretching is quantified by the Lyapunov exponent. Global mixing is quantified by the topological entropy, calculated from both defect braiding and curve extension rates. We find excellent agreement between these independent measures of chaos, demonstrating that the extensile stretching between microtubules directly translates into macroscopic braiding of positive defects. Remarkably, increasing extensile activity (via ATP concentration) does not increase the dimensionless topological entropy. This study represents the first application of chaotic advection to the emerging field of active nematics and the first time that the collective motion of an ensemble of defects has been quantified (via topological entropy) in a liquid crystal.

Nature provides many examples of active matter, ranging from flocks of birds [1], fish [2], and insects [3] to sheets of cells [4–6] and swarms of bacteria [7–9]. In the lab, various attempts have been made to develop biomimetic and synthetic active materials, from self-propelled colloids [10, 11] and mechanically agitated flocks [12], to dense phases of biopolymers driven by molecular motors [13–23]. This is a rich field of research, and to date, much theoretical work has been dedicated to understanding the fundamental physics of these fascinating and diverse systems [24, 25]. Active materials are non-equilibrium systems, and thus they cannot be described in the framework of conventional thermodynamics. The unifying theme of active matter is that collections of subunits consume energy locally, translate that energy into movement, and ultimately produce large-scale flows. This large-scale motion can produce rich emergent structures, including phase boundaries and topological defects, where local order breaks down.

The central theme of this work is the introduction of concepts from chaotic advection [26, 27] to the physics of biologically active fluids. These concepts include topological entropy and Lyapunov exponents, which are well known measures of chaos in the theory of chaotic advection but have been thus far largely overlooked in studies of active matter. Roughly speaking, the Lyapunov exponent measures the rate at which nearby fluid parcels separate from one another. The topological entropy, on the other hand, measures the asymptotic (in time) exponential growth rate in the length of a material curve as it is stretched within the fluid. We use spatially (and temporally) averaged local measurements in the fluid to estimate the Lyapunov exponent. To estimate the topological entropy, we use larger-scale measurements, including the global braiding motion of topological defects about one another.

In experimental studies of chaotic advection in passive fluids at low Reynolds number, fluid motion is often driven at the boundary, either by tangentially sliding the boundary, e.g. rotating a cylindrical boundary wall [29–31], or by directly stirring the fluid with inserted rods [28, 32–34]. The resulting chaotic flow produces exponentially stretching material curves. In stirring experiments, chaos is observed when three or more rods are inserted into the fluid and moved around one another in a braiding motion [28, 32–34]. The mathematical braid can be visualized by interpreting time as the vertical dimension. Figure 1a shows an example braid, with the initial effect of this braid on a line of dye shown schematically in Fig. 1b. Repeated applications of this stirring pattern generate an experimental image like Fig. 1c, taken from Boyland et al. [28]. The overall mixing efficiency depends on the stirring pattern, particularly on the topological braid-type of the motion, and can be quantified by the topological entropy, i.e. the growth rate of material lines as fluid elements are stretched apart from each other. One remarkable mathematical fact is that a given braid-type of the rod motion guarantees a specific minimal amount of topological entropy in the dynamics, e.g. the Fig. 1a braid generates an entropy of $\log[(1+\sqrt{5})/2] = 0.4812$ per swap of two strands. In fact, any collection of passively advected orbits in the fluid, not just those next to the stirring rods, generates a braid type, with an associated minimal topological entropy; such trajectories have been described as "ghost rods" in the literature [33, 34]. Though the mathematics is more rigorous when such trajectories are periodic in time, recent work has generalized the analysis to open, aperiodic trajectories [35–38].

Our experiments use an extensile-active-nematic fluid confined to a quasi-two-dimensional layer [15, 16, 18], Fig. 1d. The fluid consists of purified microtubules and kinesin-1 molecular motor proteins, Fig. 2a and Methods: Preparation of the 2D active nematic. In biological cells, these molecules exist in the cytoskeleton, where the microtubules form highways for the motors. The motor proteins step stochastically along a microtubule in a net direction defined by the microtubule's structural polarity, a process that consumes energy from the hydrolization of adenosine-5′-triphosphate (ATP). This force-generating action is essential for a variety of cell functions, including organelle transport [39], cell division, and cytoplasmic streaming [40].

In our laboratory setup, microtubules condense into bundles, crosslinked by clusters of streptavidin-bound kinesin motors (Fig. 2a and Methods). If two motors in a cluster bind to adjacent microtubules of opposite polarity, the opposing forces produce a sliding motion between those microtubules. Thus neighboring bundles of opposing polarity extend away from each other to generate local fluid stretching. Under the dense confinement of a 2D oil-water interface, the bundles enter the nematic phase, with a well-defined director field recording the local bundle orientation (Fig. 1d and Fig. 2b.) In the presence of ATP, the bundles continually move, extend, bend, buckle and break [15, 16, 18]. This continual motion advects individual tubulin monomers throughout the fluid in a chaotic fashion. (Supplementary Movie 1.) As a result, pairs of +1/2 and -1/2 topological defects (Fig. 1d) in the director field are continuously created and annihilated. Between their birth and death, topological defects move around one another in a complicated braiding pattern, as shown later in Fig. 3. (See also Supplementary Movie 2.)

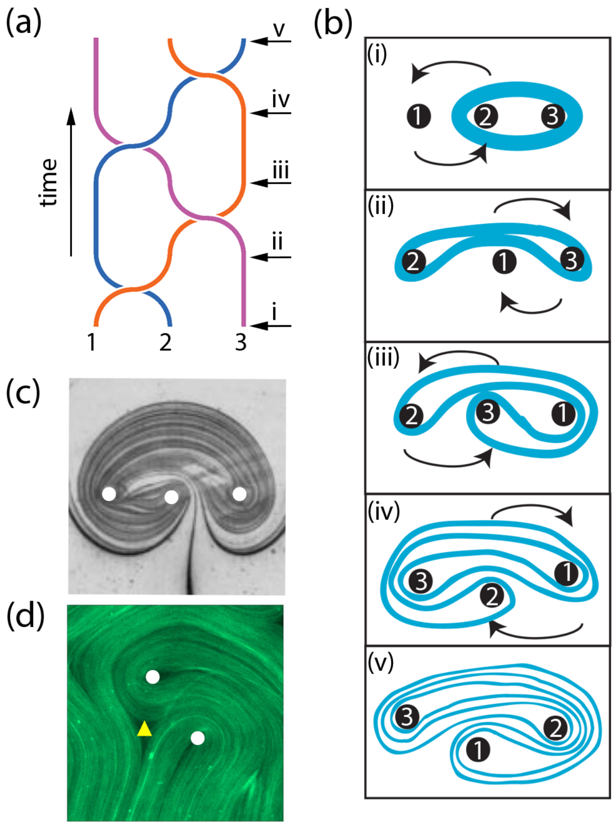

FIG. 1. Topological stirring of fluids. a) Braid diagram representing three rods as they stir a 2D fluid in a pattern known as the golden braid. Time moves up in the vertical direction. Each strand represents the world line of one rod. The time points denoted i-v correspond to the schematic in (b). b,i-v) The impact of passive stirring generated by the braid in (a) on an initial line of dye. As the rods sequentially exchange positions, the dye stretches. c) Experimental image of stirring lines of dye by three rods (adapted from Boyland et al. [28]) after several iterations of rod exchanges according to the stirring protocol shown in (a). The rod positions are highlighted in white. d) Fluorescence microscope image of the active nematic fluid with topological defects marked. White circles denote +1/2 defects; a yellow triangle denotes a -1/2 defect.

The pattern of microtubule bundles surrounding the +1/2 defects (Fig. 1d) strongly resembles the pattern of dye surrounding stirring rods (Fig. 1c) in passive advection. The active nematic fluid described here differs crucially from a conventional passive fluid in that internal flows and chaotic advection in a passive fluid must be driven externally. In this report, we show that braiding by topological defects in the active fluid produces macroscopic chaotic advection, and thus the defects act as virtual stirring rods. In addition, we demonstrate that mixing on the macroscale by virtual rods arises spontaneously as a consequence of the molecular-level sliding action. This relationship is quantified by the topological entropy and Lyapunov exponent.

One consequence of topological mixing theory is that exponential stretching cannot exist within the fluid without some nontrivial braiding of defects, as quantified by the topological entropy. It is particularly interesting that this self-driven fluid spontaneously creates a set of defects which then must move in a particular way to produce exactly the topological entropy needed to accommodate the local stretching. This observation sheds new light on prior studies of defect dynamics. For example, in the numerical work of Shendruk et al [22], they demonstrated a particular braiding pattern resembling a Ceilidh dance, in which defects braid around one another in two counter propagating lines in a channel. In fact, this particular braid has been studied in the chaotic advection literature, where it is known as the “silver braid” [34]; interestingly, it has been proved to be optimal, in that it provides the largest amount of topological entropy per time step for any linear arrangement of defects. Thus, if one were to compute the stretching rate for this flow *a priori*, one could reasonably conjecture that the Ceilidh dance pattern was topologically mandated to accommodate all the topological entropy.

We measure both the topological entropy and the Lyapunov exponent of the active flow; we measure the topological entropy using three distinct methods, designed to probe the system across different length scales. The Lyapunov exponent is obtained from the velocity-gradient tensor field, itself computed from particle-image velocimetry (PIV) using fluorescence

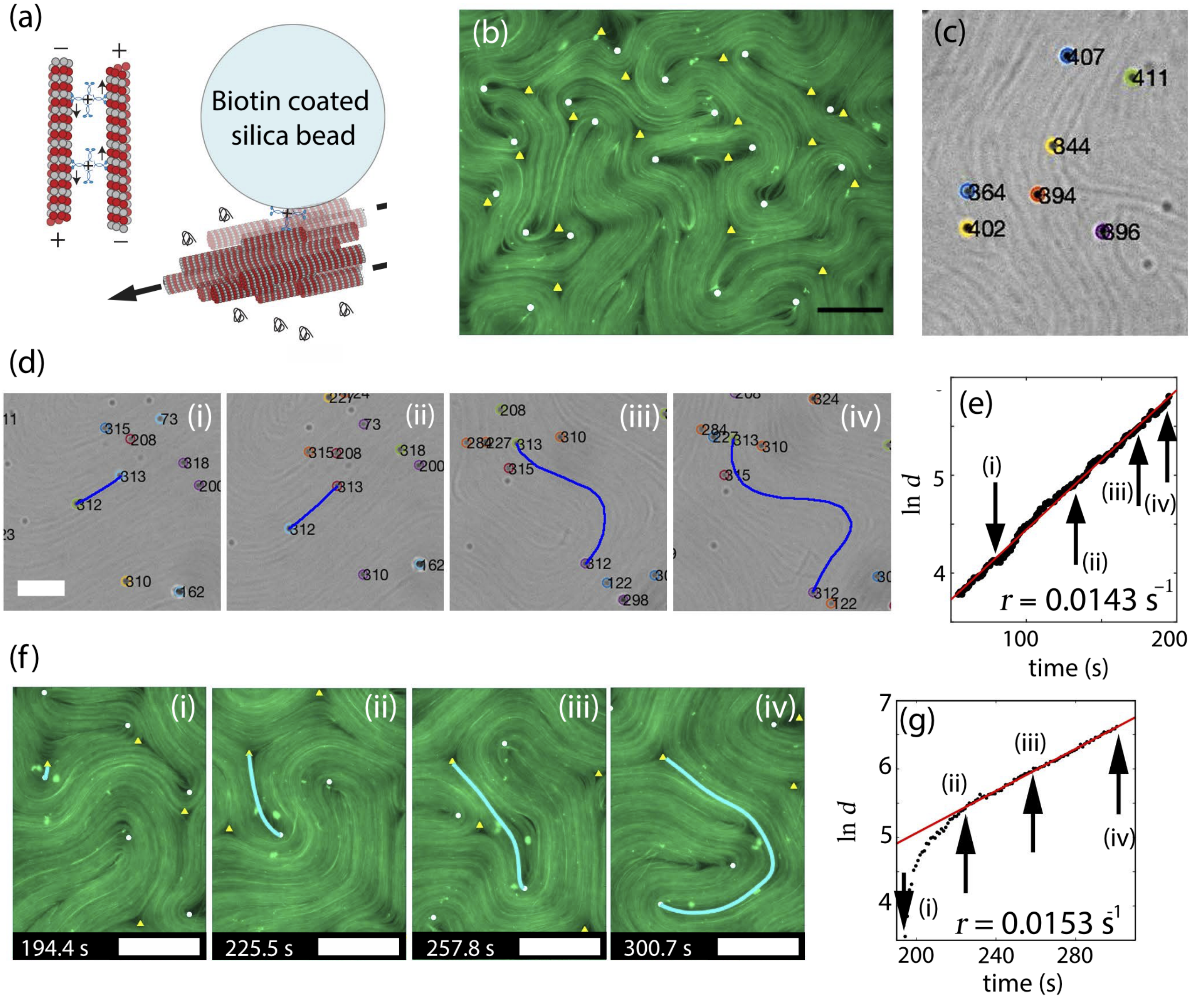

FIG. 2. Measurement of separation rates in the active fluid. (a) Schematic showing elements of the microtubule network, consisting of microtubules crosslinked by kinesin clusters. The microtubule bundles of opposite polarity extend away from each other as the kinesin motors walk. Biotin coated silica beads are used to bind onto free streptavidin binding sites in kinesin clusters to attach onto the microtubule network. (b) Fluorescence image of microtubule network in 2D at an oil-water interface with marked topological defects. White circles are +1/2 defects and yellow triangles are -1/2 defects. Scale bar, 100um. (c) Bright field image of beads attached to the microtubule network. Beads are numbered automatically for tracking. Scale bar, 25 μm. (d, i-iv) Bright field microscopy time lapse showing contour length growth between two beads moving away from each other at 50 μM ATP concentration. Scale bar, 30 μm. (e) Semi-log plot of contour length, d (microns), as a function of time for the bead pair shown in (d) with time points (i-iv) marked by arrows. We make a linear fit with slope r, inset. (f, i-iv) Time-lapse fluorescence images tracking the separation of a +1/2 defect (white) and -1/2 defect (yellow), shown by the cyan curve. Scale bar, 100 μm. (g) Semi-log plot of defect separation distance d (microns) as a function of time for a defect pair. A linear fit with slope r (inset) was made after the transient rise. The marked time points (i-iv) correspond to the images in (f).

images of the microtubule bundles. The topological entropy is measured directly using beads attached to the microtubules. As two beads pass and separate after a close approach, the exponential growth rate of the nematic contour connecting them is measured. Alternatively, the same measurement is made using the separation of neighboring topological defects. The third independent measurement of the topological entropy derives from the braiding motion of the topological defects about one another. We find that the positive topological defects act as virtual stirring rods, generating all of the topological entropy from their braiding motion; negative topological defects add very little, if any, additional entropy. The three measures of topological entropy are consistent with one another, which is remarkable given that braiding is a manifestly global and topological technique, independent of geometric details, whereas the stretching techniques depend inherently on length measurements. Furthermore, the topological entropy is slightly larger than the Lyapunov exponent, reflecting a fundamental theorem in 2D chaotic dynamics [41]. Measurements are repeated at progressively higher ATP concentrations. Increasing the ATP concentration raises the system activity, increasing the overall fluid speed. The Lyapunov exponent and topological entropy generally also increase with increasing fluid speed. We nondimensionalize these quantities to isolate the purely topological effects on mixing efficiency when we increase system activity. Across all methods we obtain a fascinating result: the dimensionless Lyapunov exponent and dimensionless topological entropy are constant with ATP concentration. This result suggests that these dimensionless quantities may be universal features of the fully developed "turbulent" state of the active nematic.

Topological entropy from bead and defect separations. We first describe the measurement of separation rate in the nematic contour joining two beads. Biotin-coated silica beads of 2μm-diameter were bound to the microtubule bundles via free binding sites on the streptavidin molecules that form the kinesin clusters. (See Fig. 2a and Methods.) This approach differs fundamentally from recent work on a similar system in which beads were passivated to *avoid* microtubule attachment, thus acting as passive tracers for the surrounding aqueous flow [15, 16]. In contrast, bound beads track the microtubule network itself. The beads move within the nematic plane, where they are imaged with bright-field optical microscopy (Fig. 2c and Supplementary Movie 3). Bead trajectories directly map the motion of microtubule segments throughout the system, including via bundle fracture and annealing.

After bead trajectories were extracted from a bright-field movie, they were searched for close approaches of bead pairs (within 2-10μm of each other). Following a close approach, the pair of beads moves apart, with a nematic contour, i.e. an integral curve of the nematic director field, stretching between them. Physically, the nematic contour represents the microtubule bundles connecting the beads; it grows and bends with the fluid as the bundles extend. For each image frame, the nematic contour was manually traced. (Fig. 2d and Supplementary Movie 4.) The slope of the natural log of the separation contour length versus time yields the separation rate r (Fig. 2e). The result shows clear exponential growth over nearly an order of magnitude in contour length. A total of nine pairs of beads were analyzed (Supplementary Fig. 1). The separation rate r is remarkably similar across bead pairs, with mean $\langle r \rangle = 0.0143$ s^{-1} and standard deviation $\sigma = 0.0016$ s^{-1}. (Supplementary Fig. 2.) To estimate the topological entropy, we perform a weighted average as discussed in Supplementary Section S1, resulting in $h_{\text{bead}} = 0.0145(\pm 0.0001)\text{s}^{-1}$.

In a second approach, we measured the separation rate between topological defects, instead of beads. Pairs of nearby $+1/2$ and $-1/2$ defects were identified in fluorescence movies. Fluorescence microscopy enhances the microtubule structure while eliminating the nonfluorescent beads. (Supplementary Movie 1.) We then identified the nematic contour between the defects as a function of time, Fig. 2f. (Supplementary Section S2.) This contour length increased exponentially (Fig. 2g), yielding the exponential separation rate r. A total of 10 defect pairs were analyzed resulting in $h_{\text{defect}} = 0.0142(\pm 0.0002)$ s^{-1} (Supplementary Fig. 3.) Results from defect and bead separations are remarkably consistent implying that the separation rate between defects is a good proxy for the growth of material curves anywhere in the fluid.

Topological entropy from defect braiding. Whereas the first two computations of topological entropy used the growth in euclidean contour length, our third approach is purely topological and independent of the first two. This approach views the topological defects as stirring rods, and computes the topological entropy by the braiding pattern of these rods around one another. (Fig. 3a.) As such, the method is insensitive to the exact positions of defects. However, the original defect trajectories must be extended to exist for all times, as described in Supplementary Section S3.

We use the recently developed E-tec algorithm [38] to extract topological entropy from defect trajectories. This algorithm uses a computational geometry approach to propagate an initial piecewise linear elastic mesh (Fig. 3b) forward in time. As trajectories evolve, the mesh is stretched and folded over itself, creating an exponentially growing number of line segments. Figure 3c shows the final stretched mesh and Fig. 3d shows the growth in the number of segments as the fluid is "stirred" by the defects. The exponential growth rate is the topological entropy generated by the stirring rods, which in general is only a lower bound to the true topological entropy of the fluid. In Navier-Stokes simulations of stirring a two-dimensional fluid, there can be significantly more entropy than that predicted by the motion of the rods.

In principle, any ensemble of trajectories passively advected in the fluid can be viewed as virtual stirring rods, and the corresponding topological entropy computed using E-tec. Again, such ensembles typically provide only a lower bound on the true entropy of the flow—the more trajectories included, the greater the lower bound. In some special cases, a small number of specifically chosen trajectories generate all of the topological entropy [38].

Figure 3d shows three results, corresponding to stirring by just the +1/2 defects, by just the -1/2 defects, and by both +1/2 and -1/2 defects. The entropy from the +1/2 defects, $0.01043(\pm 0.00080)$ s^{-1}, is significantly larger than that of the -1/2 defects, $0.00626(\pm 0.00032)$ s^{-1}. Most remarkable, however, is that the entropy from all the defects, $0.01045(\pm 0.00053)$ s^{-1}, is essentially the same as from just the positive defects. The negative de-

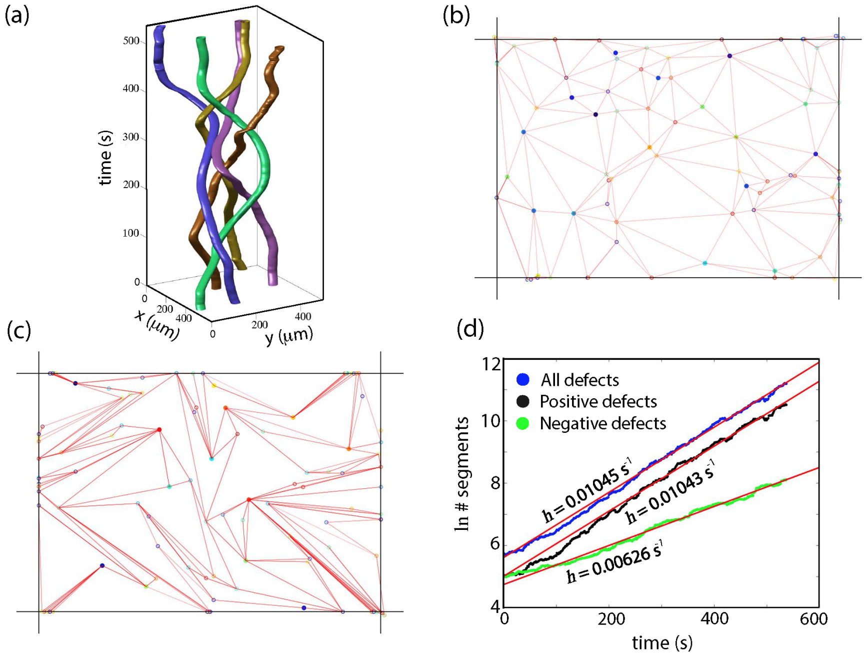

FIG. 3. E-tec computation of topological entropy. a) A sampling of positive defect trajectories braiding around one another. b) Initial mesh between defects inside the black bounding box. Filled circles are actual defects. Open circles are "extinct" defect trajectories, as discussed in the Supplementary Material. c) Final stretched mesh and defect positions. The intensity of the red segments indicates their weight. d) Plot showing topological entropy, h, calculated using the E-tec algorithm for positive defects only, 0.01043(±0.00080) s^{-1}, negative defects only, 0.00626(±0.00032) s^{-1}, and all defects, 0.01045(±0.00053) s^{-1}. Errors on the E-tec growth rates were computed as the difference in the slopes fitted over two distinct time intervals; interval 215s – 537s and interval 322s – 537s.

fects introduce no additional stretching. This is a surprisingly strong result, and shows that the positive defects are *the* special points for generating topological mixing and that they alone can account for all the topological entropy in the fluid.

Finally, the E-tec computation must be corrected for the finite size of the image domain. This correction is estimated by the escape rate of trajectories (Supplementary Section S4), which is computed from the bead data to be 0.00291(±0.00003) s^{-1}. Adding this to the E-tec result yields a final entropy $h_{\mathrm{braid}} = 0.0133(\pm 0.0008)$ s^{-1}.

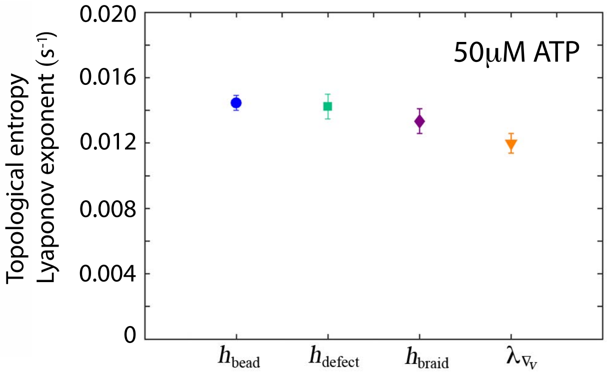

FIG. 4. Comparison of the four measures of chaos at 50μM ATP concentration. The error bars for h_{bead} and h_{defect} are the standard error of the mean, when averaging over the set of separation rates. The error on h_{braid} is essentially just that of the fit described in Fig. 3. The error on $\lambda_{\nabla\mathbf{v}}$ is based on the error of the PIV analysis, estimated at 5%. See Supplementary Section S5.

The fact that the separation-rate and braiding methods agree so well is by no means trivial or expected. Several assumptions are needed to justify that either of these methods should yield the true topological entropy. (See Supplementary Sections S1 and S4.) Such assumptions are only verified through an analysis of the experimental data. Thus, the agreement of these two measures is a significant experimental finding. For example, solid-state topologically ordered systems may have defect translation without any stretching or motion of the underlying material. In the microtubule active nematic system, the strong coupling between motion of the microtubules themselves and motion of the defects is necessary to see the agreement reported here. (This coupling only breaks down near the creation and annihilation of defect pairs. Supplementary Figs. 1e and 1f.)

Finally, we computed the Lyapunov exponent directly from the microtubule velocity field as $\lambda_{\nabla v} = 0.0120(\pm 0.0006)$ s^{-1}. (Methods: Lyapunov exponent from velocity field.) Figure 4 shows all four measures of chaos at 50μM ATP concentration. The Lyapunov exponent is slightly less than the three measurements of topological entropy. This is consistent with a general result from dynamical systems theory, which states that the topological entropy is always greater than or equal to the metric entropy (also known as the measure-theoretic or Kolomogorov-Sinai entropy) [41]. In two-dimensional area-preserving flows, the metric entropy equals the positive Lyapunov exponent, implying the relative ordering seen in Fig. 4. The fact that the Lyapunov exponent is only slightly less than the topological entropy reflects the statistical homogeneity of the active nematic flow. If the local Lyapunov exponent were constant in space and time, the topological entropy would exactly equal the Lyapunov exponent.

Variation of ATP concentration. To investigate the effects of increasing activity on chaotic advection, we ran a series of experiments at different ATP concentrations (50-1000 μM). Because ATP concentration controls the kinesin step-rate at the molecular level, we expect the topological entropy and Lyapunov exponent to increase with increasing ATP concentration.

When single microtubules glide on a kinesin-decorated glass surface, their gliding velocity as a function of ATP concentration is generally well described on a local level by Michaelis-Menten kinetics [42–44]. Similarly, we observed that the average $v_{\rm rms}$ (Methods: PIV velocity analysis) for our attached beads also follows Michaelis-Menten kinetics under ATP variation, Fig. 5a.

Henkin et al. used passive unattached tracers to measure the average bead speed in a similar, 3D microtubule network as a function of ATP concentration (0.5-3mM) [16]; they observed a monotonic increase up to 2μm/s at saturation. Our attached-bead method, however, contains richer and more direct information on the motion of the microtubules themselves.

We calculated topological entropy $h_{\rm bead}$ for bead pairs at different ATP concentrations (50–1000 μM), Fig. 5b. Separation rates were measured for $\sim$ 10 bead pairs at each concentration. (See raw data in Supplementary Fig. 2.) Though Fig. 5b shows a general upward trend, it is not strictly monotonic. For context, we consider the relevant physical scales. An inverse-time scale τ^{-1} for $h_{\rm bead}$ can be obtained by combining the characteristic velocity $v_{\rm rms}$ with a characteristic length ℓ. Following Refs. [23, 45], we chose ℓ to be the length at which the velocity-velocity correlation function, computed from PIV velocities, decays to half its maximum value, Fig. 5c. (Methods: PIV velocity analysis.) ℓ varies only modestly with ATP concentration, consistent with Lemma et al [23] for ATP concentrations larger than 10μM. Refs. [23, 45] establish that the correlation length ℓ arises from balancing the elastic bend energy of the microtubule bundles with motor activity. Thus, if only the activity were increased, ℓ should decrease, and indeed, except for the 250 μM data, our results are consistent with a small downward trend. The outlier at 250 μM ATP concentration could be understood by a slight change in the microtubule lengths, which would affect the correlation length. Microtubule bundle length is very sensitive to sample preparation, such as pipette shearing.

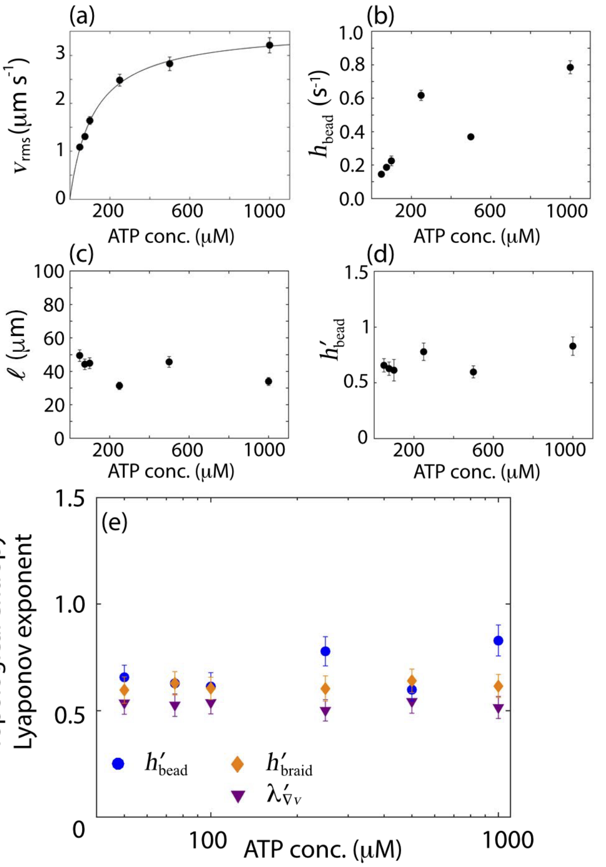

FIG. 5. Nondimensionalized topological entropy and Lyapunov exponent are insensitive to motor activity. a) Average $v_{\rm rms}$ of beads as a function of ATP concentration. This relationship follows Michaelis-Menten kinetics (solid curve) $v = (v_{\max} \times [ATP])/([ATP] + K_m)$ with fit parameters $K_m = 120(\pm 20)$ μM and $v_{\max} = 3.57(\pm 0.19)\mu$m/s. b) Topological entropy computed from bead separation as a function of ATP concentration. c) Velocity correlation length ℓ, as a function of ATP concentration. d) Dimensionless topological entropy $h'_{\rm bead}$ versus ATP concentration. This was obtained by multiplying the original entropy $h'_{\rm bead}$ in (b) by the characteristic time derived from plots (a) and (c). e) All four dimensionless measures of chaos as a function of ATP concentration. Error bars on the dimensionless measures include the errors on the characteristic length and velocity, which combine to give an error on the time scale $\Delta\tau = \tau[(\Delta\ell/\ell)^2 + (\Delta v_{\rm rms}/v_{\rm rms})^2]^{1/2}$. The error on $h'_{\rm bead}$, for example, is then $\Delta h'_{\rm bead} = h'_{\rm bead}[(\Delta h_{\rm bead}/h_{\rm bead})^2 + (\Delta\tau/\tau)^2]^{1/2}$.

We obtain the dimensionless topological entropy $h'_{\rm bead} = \tau h_{\rm bead}$ by rescaling by the characteristic time $\tau = \ell/v_{\rm rms}$, Fig. 5d. This scales out any fluctuations in either ℓ or $v_{\rm rms}$ due to experimental factors, resulting in a measure of topological entropy that depends only on the flow geometry. Surprisingly, the dimensionless entropy $h'_{\rm bead}$ is nearly constant with ATP concentration; although the system moves faster with increased ATP, the underlying geometric complexity of the mixing remains constant. This suggests that the dimensionless topological entropy may be a universal quantity for the fully "turbulent" state of active nematics.

For each ATP concentration, we also computed the other measures of chaos. The two separation-based entropies are in close agreement. (Supplementary Fig. 5.) Figure 5e thus shows just the bead-separation entropy compared to the other two measures. Again, each dimensionless measure varies little with ATP. The average of the bead entropy is $\langle h'_{\rm bead}\rangle = 0.684$, with braiding entropy somewhat lower at $\langle h'_{\rm braid}\rangle = 0.614$. As expected, the Lyapunov exponent, $\langle \lambda'_{\nabla v}\rangle = 0.526$, is below all measures of topological entropy. There are two main reasons why $\langle h'_{\rm braid}\rangle$ may be lower than $\langle h'_{\rm bead}\rangle$. First, the estimate of the finite-size effect of the image domain may fail to account for the full complexity of braiding near the boundary. Second, the "extinct" defects that exist before and after defect creation and annihilation events are passively advected by the PIV velocity field, which has some error in the velocity component along the director.

Active fluids have emerged as an exciting frontier in soft matter physics, but until now, their flows have not been examined in detailed experiments from the perspective of chaotic dynamics. Using this approach, we have investigated the spontaneous "self-mixing" of an extensile active nematic.

It is well-appreciated that energy injected by molecular motors into active nematics at the molecular scale produces large-scale flows. Our results support the complementary view that fluid *stretching* is also injected into the flow of an active nematic at the molecular scale. This stretching can be quantified by the Lyapunov exponent. The fluid flow must respond on the macroscale in a manner consistent with this local stretching. Consistency requires that the $+1/2$ defects, which drive the stirring, braid around one another in a manner sufficiently complex to produce topological entropy greater than the Lyapunov exponent. The number, density, and speed of the defects are not sufficient, in themselves, to produce topological entropy. The braiding pattern is critical. Our data demonstrate that the topological entropy of the moving defects is greater than the stretching injected via kinesin-motor-driven filament sliding; the excess entropy, i.e. the difference between topological entropy and the Lyapunov exponent, is shown to be quite small, reflecting the homogeneity of the fluid motion.

In total, four different chaotic mixing measurements are taken across a range of activity levels (tuned via ATP concentration) to calculate the topological entropy and Lyapunov exponents. The results are consistent across all four techniques. Remarkably, when non-dimensionalized, these quantities do not depend significantly on ATP concentration. This suggests that the dimensionless topological entropy and/or Lyapunov exponent of this system may be a universal feature of the "turbulent" state of such systems. It would be interesting to probe this hypothesis by varying other parameters, such as kinesin density or oil viscosity. It would also be interesting to probe the topological entropy as the system evolves across the transition from the non-turbulent to the fully "turbulent" state. For example, is the rise in topological entropy sharp or gradual?

Finally, we propose that this microtubule/kinesin system can be considered as a chemically-driven self-mixing fluid, opening the door for a potential new class of non-equilibrium energy-dissipative solvents.

Acknowledgements. Our group is grateful to Prof. Zvonimir Dogic for the generous contribution of microtubules and molecular motors and to Linnea Metcalf for sample preparation. We would also like to acknowledge useful discussions with Prof. Suzanne Sindi. The authors acknowledge generous funding from the National Science Foundation, through several awards: DMR-1808926, NSF-CREST: Center for Cellular and Biomolecular Machines at UC Merced (HRD-1547848) and from the Brandeis Biomaterials facility MRSEC-1420382.

Contributions. LSH and KAM designed the study. AJT carried out the experiments. AJT, ER, SAS, UA, JA, SF, and KAM performed analysis. LSH, KAM, and AJT wrote the paper.

Data Availability Statement: The data that support the findings of this study are available from the corresponding authors upon reasonable request.

---

[1] Toner, J. & Tu, Y. Long-range order in a two-dimensional dynamical XY model: How birds fly together. *Phys. Rev. Lett.* **75**, 4326–4329 (1995).

[2] Katz, Y., Tunstrøm, K., Ioannou, C. C., Huepe, C. & Couzin, I. D. Inferring the structure and dynamics of interactions in schooling fish. *Proceedings of the National Academy of Sciences* **108**, 18720–18725 (2011).

[3] Buhl, J. *et al.* From disorder to order in marching locusts. *Science* **312**, 1402–1406 (2006).

[4] Saw, T. B. *et al.* Topological defects in epithelia govern cell death and extrusion. *Nature* **544**, 212 (2017).

[5] Kawaguchi, K., Kageyama, R. & Sano, M. Topological defects control collective dynamics in neural progenitor cell cultures. *Nature* **545**, 327 (2017).

[6] Prost, J., Jülicher, F. & Joanny, J.-F. Active gel physics. *Nature Physics* **11**, 111 (2015).

[7] Sokolov, A., Aranson, I. S., Kessler, J. O. & Goldstein, R. E. Concentration dependence of the collective dynamics of swimming bacteria. *Phys. Rev. Lett.* **98**, 158102 (2007).

[8] Wensink, H. H. *et al.* Meso-scale turbulence in living fluids. *Proceedings of the National Academy of Sciences* **109**, 14308–14313 (2012).

[9] Dunkel, J. *et al.* Fluid dynamics of bacterial turbulence. *Phys. Rev. Lett.* **110**, 228102 (2013).

[10] Palacci, J., Sacanna, S., Steinberg, A. P., Pine, D. J. & Chaikin, P. M. Living crystals of light-activated colloidal surfers. *Science* **339**, 936–940 (2013).

[11] Yan, J. *et al.* Reconfiguring active particles by electrostatic imbalance. *Nature Materials* **15**, 1095 (2016).

[12] Narayan, V., Menon, N. & Ramaswamy, S. Nonequilibrium steady states in a vibrated-rod monolayer: tetratic, nematic, and smectic correlations. *Journal of Statistical Mechanics: Theory and Experiment* **2006**, P01005 (2006).

[13] Ndlec, F. J., Surrey, T., Maggs, A. C. & Leibler, S. Self-organization of microtubules and motors. *Nature* **389**, 305 (1997).

[14] Schaller, V., Weber, C., Semmrich, C., Frey, E. & Bausch, A. R. Polar patterns of driven filaments. *Nature* **467**, 73 (2010).

[15] Sanchez, T., Chen, D. T. N., DeCamp, S. J., Heymann, M. & Dogic, Z. Spontaneous motion in hierarchically assembled active matter. *Nature* **491**, 431 (2012).

[16] Henkin, G., DeCamp, S. J., Chen, D. T. N., Sanchez, T. & Dogic, Z. Tunable dynamics of microtubule-based active isotropic gels. *Philosophical Transactions of the Royal Society of London A: Mathematical, Physical and Engineering Sciences* **372** (2014).

[17] Giomi, L. Geometry and topology of turbulence in active nematics. *Phys. Rev. X* **5**, 031003 (2015).

[18] DeCamp, S. J., Redner, G. S., Baskaran, A., Hagan, M. F. & Dogic, Z. Orientational order of motile defects in active nematics. *Nature Materials* **14**, 1110 (2015).

[19] Guillamat, P., Ignés-Mullol, J. & Sagués, F. Control of active liquid crystals with a magnetic field. *Proceedings of the National Academy of Sciences* **113**, 5498–5502 (2016).

[20] Doostmohammadi, A., Shendruk, T. N., Thijssen, K. & Yeomans, J. M. Onset of meso-scale turbulence in active nematics. *Nature Communications* **8**, 15326 (2017).

[21] Guillamat, P., Ignés-Mullol, J. & Sagués, F. Taming active turbulence with patterned soft interfaces. *Nature Communications* **8**, 564 (2017).

[22] Shendruk, T. N., Doostmohammadi, A., Thijssen, K. & Yeomans, J. M. Dancing disclinations in confined active nematics. *Soft Matter* **13**, 3853–3862 (2017).

[23] Lemma, L. M., DeCamp, S. J., You, Z., Giomi, L. & Dogic, Z. Statistical properties of autonomous flows in 2d active nematics. *Soft Matter* **15**, 3264–3272 (2019).

[24] Ramaswamy, S. The mechanics and statistics of active matter. *Annual Review of Condensed Matter Physics* **1**, 323–345 (2010).

[25] Marchetti, M. C. *et al.* Hydrodynamics of soft active matter. *Rev. Mod. Phys.* **85**, 1143–1189 (2013).

[26] Aref, H. Stirring by chaotic advection. *Journal of Fluid Mechanics* **143**, 1–21 (1984).

[27] Aref, H. *et al.* Frontiers of chaotic advection. *Rev. Mod. Phys.* **89**, 025007 (2017).

[28] Boyland, P. L., Aref, H. & Stremler, M. A. Topological fluid mechanics of stirring. *J. Fluid Mech.* **403**, 277–304 (2000).

[29] Muzzio, F. J., Swanson, P. D. & Ottino, J. M. The statistics of stretching and stirring in chaotic flows. *Physics of Fluids A: Fluid Dynamics* **3**, 822–834 (1991).

[30] Chaiken, J., Chevray, R., Tabor, M., Tan, Q. M. & Stuart, J. T. Experimental study of lagrangian turbulence in a stokes flow. *Proceedings of the Royal Society of London. A. Mathematical and Physical Sciences* **408**, 165–174 (1986).

[31] Aref, H. & Balachandar, S. Chaotic advection in a stokes flow. *The Physics of Fluids* **29**, 3515–3521 (1986).

[32] Vikhansky, A. Chaotic advection of finite-size bodies in a cavity flow. *Physics of Fluids* **15**, 1830–1836 (2003).

[33] Gouillart, E., Thiffeault, J.-L. & Finn, M. D. Topological mixing with ghost rods. *Phys. Rev. E* **73**, 036311 (2006).

[34] Finn, M. D. & Thiffeault, J.-L. Topological optimization of rod-stirring devices. *SIAM Review* **53**, 723–743 (2011).

[35] Thiffeault, J.-L. Braids of entangled particle trajectories. *Chaos* **20** (2010).

[36] Allshouse, M. R. & Thiffeault, J.-L. Detecting coherent structures using braids. *Physica D: Nonlinear Phenomena* **241**, 95 – 105 (2012).

[37] Budišić, M. & Thiffeault, J.-L. Finite-time braiding exponents. *Chaos* **25** (2015).

[38] Roberts, E., Sindi, S., Smith, S. A. & Mitchell, K. A. Ensemble-based topological entropy calculation (e-tec). *Chaos: An Interdisciplinary Journal of Nonlinear Science* **29**, 013124 (2019).

[39] Hirokawa, N., Noda, Y., Tanaka, Y. & Niwa, S. Kinesin superfamily motor proteins and intracellular transport. *Nature Reviews Molecular Cell Biology* **10**, 682 (2009).

[40] Lu, W., Winding, M., Lakonishok, M., Wildonger, J. & Gelfand, V. I. Microtubule–microtubule sliding by kinesin-1 is essential for normal cytoplasmic streaming in drosophila oocytes. *Proceedings of the National Academy of Sciences* **113**, E4995–E5004 (2016).

[41] Young, L.-S. Entropy in dynamical systems. In *Entropy*, 313–327 (Princeton University Press Princeton, NJ, 2003).

[42] Visscher, K., Schnitzer, M. J. & Block, S. M. Single kinesin molecules studied with a molecular force clamp. *Nature* **400**, 184–189 (1999).

[43] Lam, A. T., Curschellas, C., Krovvidi, D. & Hess, H. Controlling self-assembly of microtubule spools via kinesin motor density. *Soft Matter* **10**, 8731–8736 (2014).

[44] Tan, A. J., Chapman, D. E., Hirst, L. S. & Xu, J. Understanding the role of transport velocity in biomotor-powered microtubule spool assembly. *RSC Adv.* **6**, 79143–79146 (2016).

[45] Hemingway, E. J., Mishra, P., Marchetti, M. C. & Fielding, S. M. Correlation lengths in hydrodynamic models of active nematics. *Soft Matter* **12**, 7943–7952 (2016).

[46] Thielicke, W. & Stamhuis, E. J. PIVlab – towards user-friendly, affordable and accurate digital particle image velocimetry in MATLAB. *Journal of Open Research Software* **2**, e30 (2014).

[47] Crocker, J. C. & Grier, D. G. Methods of digital video microscopy for colloidal studies. *Journal of Colloid and Interface Science* **179**, 298 – 310 (1996).

Methods. *Flow cell preparation.* Flow cells for the experiments are constructed from a hydrophilic cover slip and a hydrophobic glass microscope slide as described by Sanchez et al. [15]. This treatment facilitates formation of the oil and water layers necessary for sample preparation. The two surfaces are treated differently so that we can flow oil and water into the flow cell (Supplementary Figure 6). First, the coverslips are treated with a polyacrylamide brush that allows the surface to be hydrophilic and prevent non-specific binding of proteins [15]. The coverslips are washed with soap and hot water, then rinsed with water three times. The coverslips are submerged in ethanol, rinsed with water, and submerged in 0.1M NaOH and rinsed with water. Once the coverslips are cleaned, they are placed in a solution containing 98.5% ethanol, 1% acetic acid and 0.5% silane-bonding agent 3-(trimethoxysilyl)propylmethacrylate (Arcos Organics) for 15 minutes. The coverslips are rinsed with water before immersion in an acrylamide solution containing 2% (w/v%) acrylamide, 35 μl per 100 ml of TEMED (Bio-Rad) and 70mg per 100ml of ammonium persulfate. This helps polymerization of the polyacrylamide brush on the surface of the coverslips. The coverslips are stored in this acrylamide gel. Before immediate use, the coverslips are rinsed with water and air-dried. The glass slides are washed with acetone, methanol and ethanol. The slides are then treated with Aquapel to create a hydrophobic surface. About 50μl of Aquapel glass treatment is dropped onto a glass slide. A second glass slide is placed on top perpendicular to the first slide to spread the solution evenly onto both surfaces and left to sit for one minute. The slides are then dried with compressed air, rinsed with water, and air-dried before use.

Preparation of the 2D active nematic. Microtubule polymerization was carried out and kinesin-streptavidin clusters prepared as previously reported by the Dogic Lab [15]. Biotin-coated 2μm-diameter silica beads (Nanocs) are diluted to 5000 beads/μl in M2B buffer (80mM PIPES pH 6.8, 2mM MgCl$_2$, 1mM EGTA) and bath sonicated for 30 minutes to one hour to break up bead aggregates. An active premixture containing biotin-kinesin, streptavidin, PEG (poly(ethylene glycol)), and PKLDH (an ATP regenerating system) is prepared as previously described in Sanchez et al. [15]. Two antioxidant mixtures are used along with Trolox to avoid photobleaching during the imaging. Antioxidant solution AO1 contains 150 mg ml^{-1} glucose and 250 mM DTT. Antioxidant solution AO2 contains 10 mg ml^{-1} glucose oxidase and 1.75 mg ml^{-1} catalase. The kinesin-streptavidin motor clusters (KSA) are made by combining 0.31 mg ml^{-1} K401 kinesin motors, 0.18 mg ml^{-1} streptavidin, and 2.2 μg ml^{-1} DTT and incubated on ice for 30 min. This mixture is diluted with M2B in the ratio 1:8.6. A high-salt buffer (MIX) is prepared containing 69mM MgCl$_2$ diluted in M2B. The ATP-regenerating system is prepared with 917 units/ml pyruvate kinase and 913 units/ml lactate dehydrogenase in aqueous buffered glycerol solution (PKLDH). The final premixture is combined by adding 1.33 μl AO1, 1.33 μl of AO2, 1.7 μl PKLDH, 2.9 μl MIX, 4 μl KSA, 6 μl 20mM Trolox, 8 μl 200mM phosphoenolpyruvate, 8 μl 6% (w/v %) 20kD PEG. The premixture is separated into 6.64 μl aliquots. To form the active network, we take one aliquot of the premixture and add ATP (50-1000μM) and fill to 10 μl with M2B. Then 2 μl of 6 mg ml^{-1} of Alexa-647 labeled GMPCPP microtubules ($\sim$ 3% labeling) is added to the 10μl of premixture. The mixture is incubated for 5-30 minutes at room temperature to allow the network to form. The network takes longer to form for lower ATP concentrations. Finally, 0.5μl of the silica bead solution is added to the microtubule network and gently tapped to mix. A 6 μl volume flow cell is created by first placing strips of double-sided tape about 3 mm apart on a hydrophobic Aquapel treated glass slide. Then, an acrylamide coated coverslip is placed on top to create a channel open at both ends (Supplementary Figure 6). To create the active microtubule layer, we first flow an oil/surfactant mixture (HFE7500 with 1.8% (v/v %) PFPE-PEG-PFPE surfactant) into the channel. Then we immediately exchange the oil/surfactant mixture by flowing in the aqueous component containing the active microtubule network including the biotin beads. The flow cell is sealed with UV-curable glue (RapidFix). To confine the active network into a quasi-2D layer, we place the filled flow cell into a swinging bucket rotor (Sorvall Legend RT+ centrifuge, four place swinging bucket rotor), and spin the material down for 42 min at 350 rpm. This step allows the active fluid to assemble at the oil/water interface inside the flow cell.

PIV velocity analysis. Particle image velocimetry (PIV) analysis was carried out with the Matlab PIVlab 1.43 package [46], using the default GUI settings. PIVLab uses sequential images to calculate a velocity vector field for each frame. We analyzed both bright-field and fluorescence movies at every ATP concentration. For each experimental run, $v_{\rm rms}$ was computed in the center of velocity frame. We calculated the average velocity vector in each frame and subtracted it from every velocity vector in the frame to obtain the velocity field in the center of velocity frame. We then calculated the resulting root-mean-squared velocity for each frame, and averaged over all frames for the final $v_{\rm rms}$ value.

We also used the PIV velocities to compute the velocity-velocity correlation length for each data run, as in Ref. [23, 45]. The velocity autocorrelation function was computed as $C(r) = \sum_{ij} \hat{\mathbf{v}}_i \cdot \hat{\mathbf{v}}_j \delta(r - r_{ij})$, where the indices i and j range over all frames and all grid points within a frame, $\hat{\mathbf{v}}_i = \mathbf{v}_i/|\mathbf{v}_i|$ is the unit velocity vector, and $r_{ij} = |\mathbf{r}_i - \mathbf{r}_j|$, for grid points $\mathbf{r}_i$ and $\mathbf{r}_j$. Numerically, the delta function is approximated as a rectangle. The correlation length was taken to be the distance at which the correlation function $C(r)$ decayed to half its value at $r = 0$.

Imaging and analysis. The active nematic is imaged using a (Leica DMP) fluorescence microscope and a Qimage Retiga Exi camera. Fluorescence movies are recorded with a 500ms exposure time per frame and a 100ms time interval between frames. The bright field movies of the beads are recorded using a 10ms exposure per frame with 100ms intervals between frames. We used a MatLab adapted tracking algorithm to track bead trajectories [47]. The bead attachment was very stable over the timescale of a typical experiment. Any unbound beads were easy to distinguish and eliminate from the analysis due to their characteristic Brownian motion and tendency to sediment to the glass surface when centrifuged. Any bead clusters were also eliminated from the analysis. To measure the separation distance between beads with diverging trajectories, we used the segmented line tool in ImageJ to measure the nematic contour length between beads for each successive frame throughout the movie.

Computation of director field and topological defect locations. We wrote Matlab code to compute the director at each grid point using a windowed Fourier transform. A Gaussian filter was first applied to the image, centered on the selected grid point. The Fourier transform of the filtered image was then applied, followed by a second Gaussian filter on the radius in Fourier space. The covariance matrix of the resulting distribution in Fourier space was then computed, and the director was taken to point along the largest eigenvector.

Topological defects were identified by regions of rapid rotation of the director field. Specifically, we identified isolated patches of grid points in the image domain in which the change in the director was large ($\delta\theta \geq \pi/4$) between neighboring grid points. The topological charge for each such patch was computed from $\Delta\theta/(2\pi)$, summed along the loop surrounding, but just outside, the patch, thereby guaranteeing that $\delta\theta < \pi/4$ between successive grid points.

Lyapunov exponent from velocity field. We computed the Lyapunov exponent directly from the microtubule velocity field. We used particle image velocimetry (specifically the MATLAB PIVLab package [46]) to compute the velocity as a function of position and time from the fluorescence movie. A local Lyapunov exponent can then be computed at each point in space and time as the parallel derivative of the parallel component of velocity, where parallel is with respect to the nematic director. (Supplementary Section S5.) Averaging over space and time yields the Lyapunov exponent $\lambda_{\nabla v}$. (Recent work [17, 21, 23] has also used the PIV velocity gradient as a system diagnostic to detect vortices using the Okubo-Weiss field $-\det(\nabla \mathbf{v})$.) In practice, the PIV analysis produces a more reliable component of velocity in the direction perpendicular to the nematic director than parallel to it. We thus compute the Lyapunov exponent $\lambda_{\nabla v} = 0.0120(\pm 0.0006)\ \mathrm{s}^{-1}$ as the average of (minus) the *perpendicular* derivative of the *perpendicular* component of velocity $\mathbf{v}$. These two averages are equal so long as the system is area-preserving (on average.)

Code availability statement. The Matlab code for computing nematic director fields and topological defects is available upon request from KAM. The E-tec code is available in python from SAS upon request.

Supplementary Material

S1. COMPUTATION OF TOPOLOGICAL ENTROPY FROM SEPARATION DATA

For two-dimensional fluid flows, topological entropy is the exponential growth rate of a material curve embedded in the fluid, in the limit that time goes to infinity, at which point the nematic contour connecting the beads would fill in the entire fluid domain. Due to the open boundary of the present experimental system, we can not track a material curve indefinitely, because some piece of it will eventually leave the field of view. There are other complications as well. When tracking a curve between bead pairs, beads may fail to be identified or properly classified in the tracking data, for one or more frames; when tracking a curve between defects, the defects may annihilate.

We address these obstacles by measuring the expansion rate for a sampling of multiple shorter segments, and then averaging. Assume that a single long curve is broken into n pieces of length L_k so that the total length is $L = \sum_{k=1}^{n} L_k$. For each individual piece, we fit an exponential so that $\ln L_k(t) \approx r_k t + \ln L_k(0)$, where the r_k's are the separation rates between the initial and final points of each piece. Supplementary Fig. 1 shows examples of this fitting for both bead and defect separations. A summary of the measured separation rates are shown in Supplementary Fig. 2 for all bead pairs and Supplementary Fig. 3 for all defect pairs. Then, the full topological entropy can be approximated as

$$h \approx \frac{dL(t)/dt}{L(t)} = \frac{\sum_k dL_k(t)/dt}{\sum_k L_k(t)} \approx \frac{\sum_k L_k(t) r_k}{\sum_k L_k(t)} \approx \frac{\sum_k L_{kf} r_k}{\sum_k L_{kf}} = \sum_k w_k r_k, \tag{1}$$

where L_{kf} is the length of the segment L_k at the final time of the fit interval and $w_k = L_{kf}/\sum_k L_{kf}$. That is, we choose the largest time for each individual segment, so that h is just the mean of the individual r_k's, weighted by the final lengths L_{kf} of the measured curves. This averaging approach assumes that a sufficient number of short curves n has been selected to sufficiently sample their spatial variation. It also assumes that the separation-rate statistics are uniform in time. We compute the error on the topological entropy h as $\Delta h = \sigma/\sqrt{n}$, where σ is the weighted standard deviation $\sqrt{\sum_k w_k r_k^2 - h^2}$.

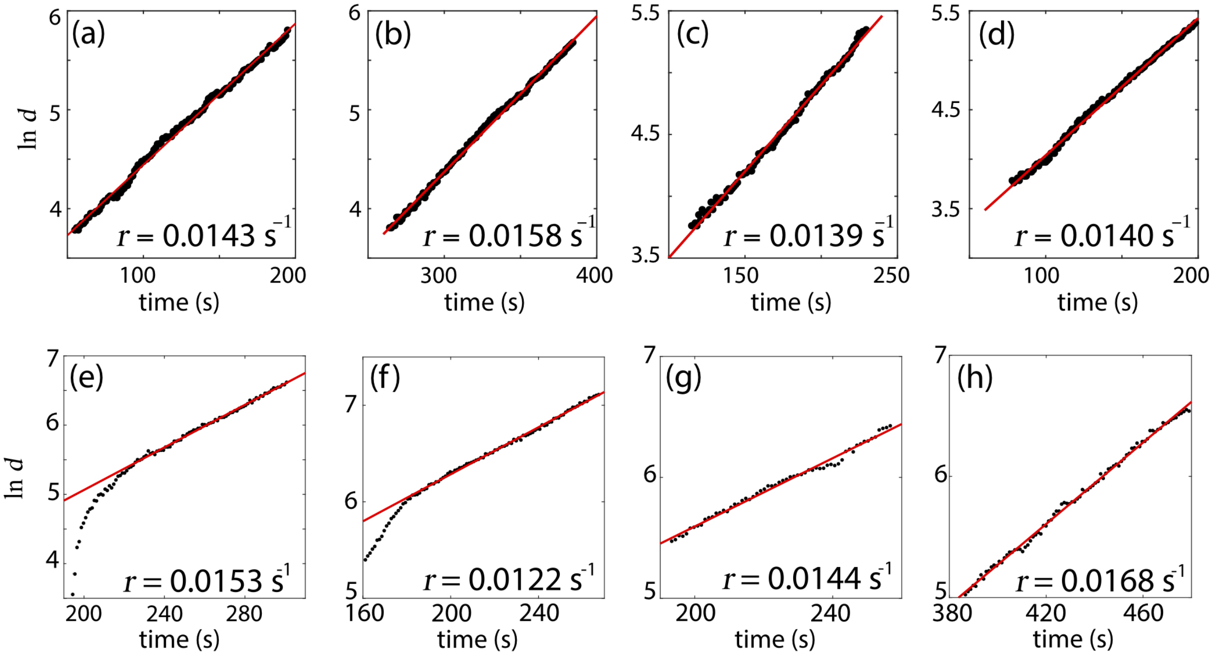

FIG. S1. (a-d) Semi-log plots of contour length, d, as a function of time for four separating bead pairs at 50 μM ATP concentration. Slopes for each plot are inset. (e-h) Semi-log plots of defect separation contour lengths as a function of time for four defect pairs at 50 μM ATP concentration, with slopes r inset. Panels (e) and (f) show an initial rapid rise immediately after pair creation, in which defects move apart before the onset of exponential stretching. The linear fit is made after this transient behavior.

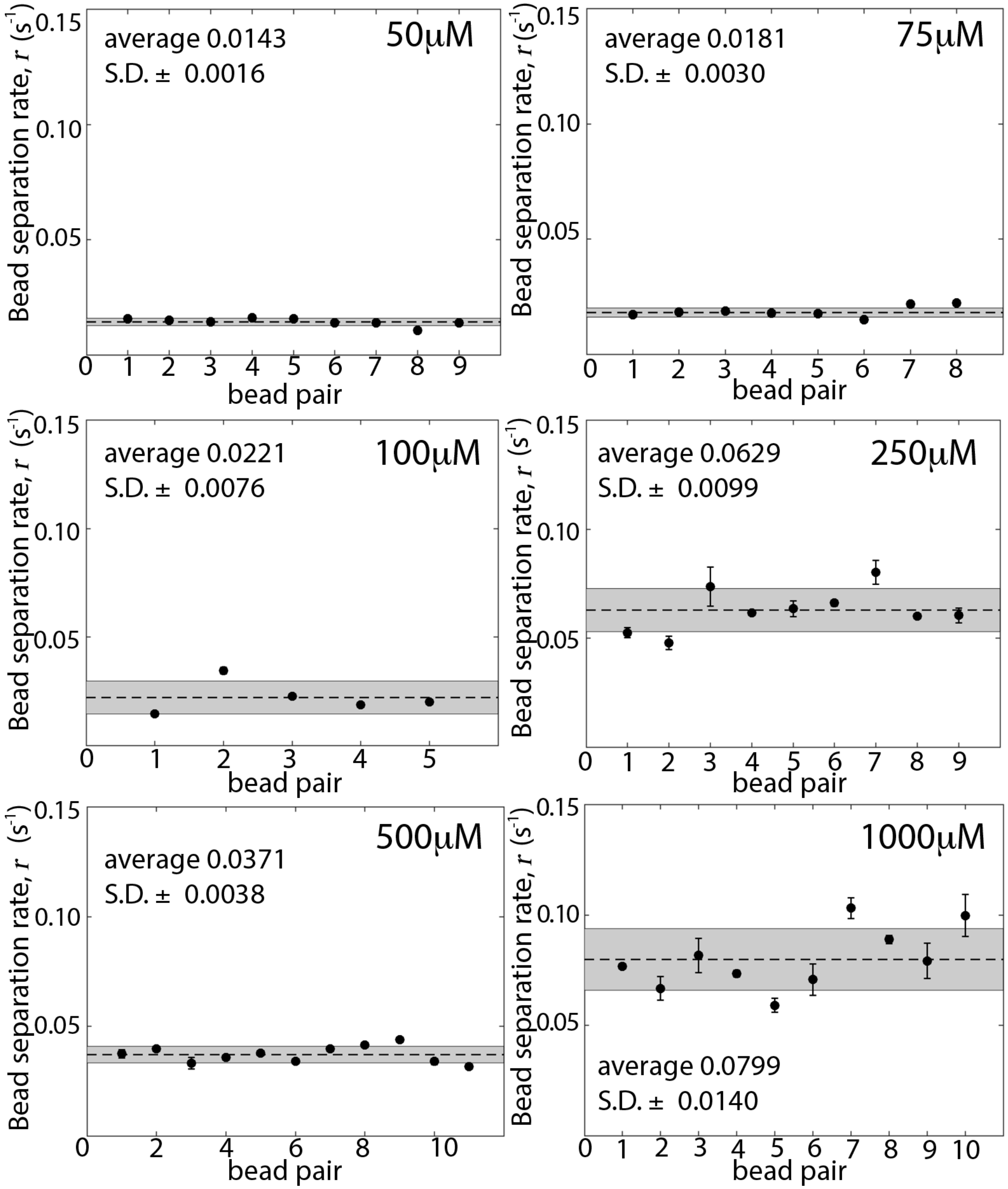

FIG. S2. The spread of the separation rate measured for each bead pair for all ATP concentrations (50-1000μM). The dotted line indicates the average separation rate for each corresponding ATP concentration and the shaded grey region indicates the standard deviation.

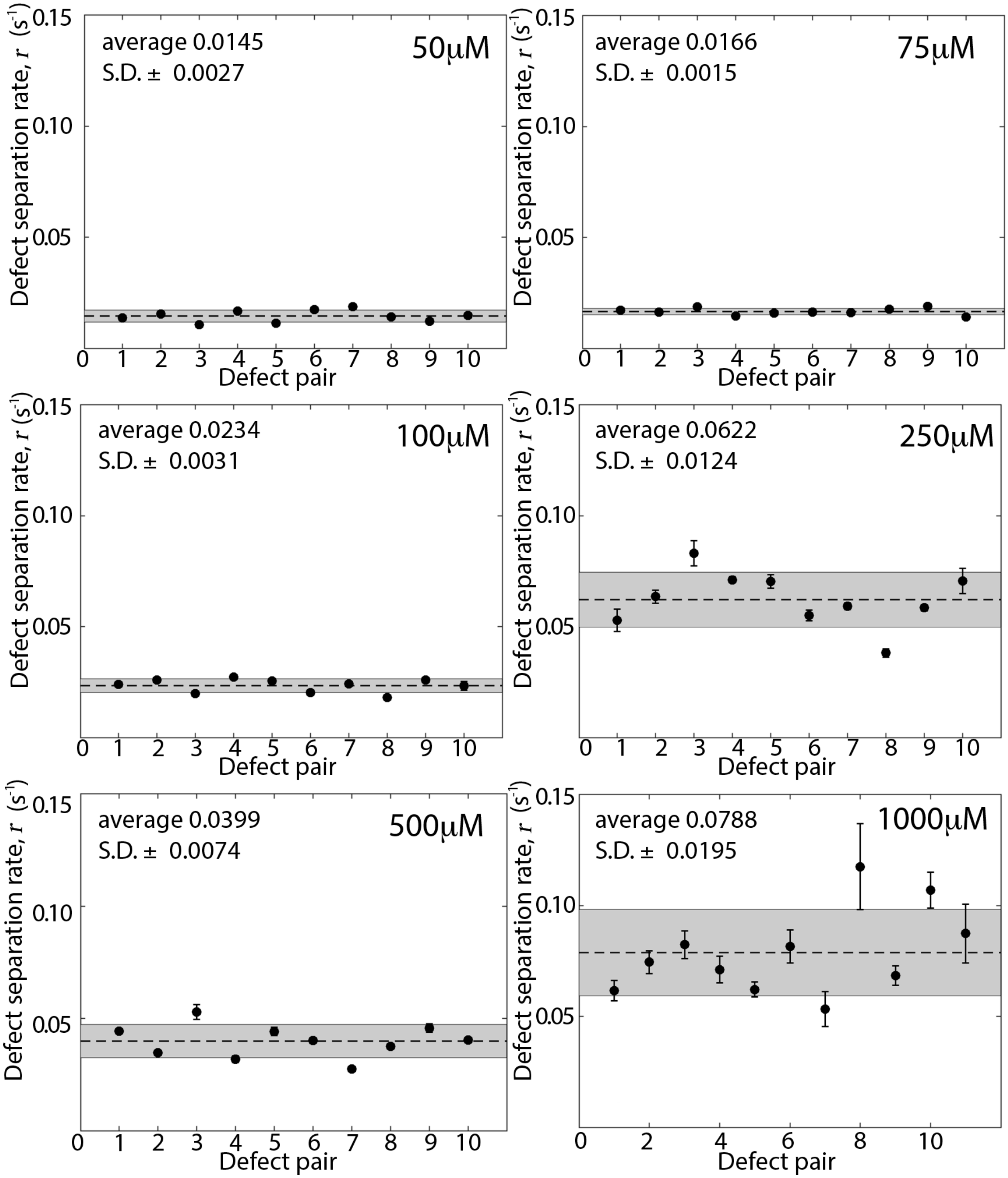

FIG. S3. The spread of the separation rate measured for each defect pair for all ATP concentrations (50-1000 μM). The dotted line indicates the average separation rate for each corresponding ATP concentration and the shaded grey region indicates the standard deviation.

S2. MEASUREMENT OF DEFECT SEPARATION RATES.

We recorded the fluorescence movie (Supplementary Movie 1) immediately after the bright-field movie of the same experimental sample. Fluorescence microscopy enhances the microtubule structure while eliminating the nonfluorescent beads. We then processed the fluorescence images to automatically extract the nematic director field and associated topological defects. (See Methods: Computation of director field and topological defect locations; also Fig. 2b and Supplementary Movie 2). Defects were tracked using the same software used for beads [47]. Pairs of nearby $+1/2$ and $-1/2$ defects were then selected, and the nematic contour joining them was integrated from the director field as the defects separated. (Fig. 2f and Supplementary Movie 5.) Figure 2g shows the natural log of the contour length versus time. One difference between defect and bead separation data is that the defect separation often exhibits a slow transient immediately following creation of the defect pair. The linear fit is made after this transient dies out. Supplementary Fig. 1e-1h shows four examples, which exhibit clear exponential growth with similar separation rates r. A total of 10 defect pairs were analyzed with mean $\langle r \rangle = 0.0145\ \mathrm{s}^{-1}$ and standard deviation $\sigma = 0.0027\ \mathrm{s}^{-1}$. (See Supplementary Fig. 2.) The topological entropy is estimated by weighting the separation rates as discussed above. The result from defect separation is remarkably consistent with that of bead separation. This implies that the separation rate between defects is a good proxy for the growth of material curves anywhere in the fluid, which means the separation rate could be extracted from other experimental runs in which only fluorescence images were available.

S3. EXTENSION OF DEFECT TRAJECTORIES.

When a positive and negative defect annihilate, we insert two "extinct" defects that are passively advected in the fluid using the PIV velocity field. The same applies going backward in time when two defects are born. Furthermore, when a defect (or extinct defect) strikes the boundary of the image domain, the trajectory is fixed to the boundary and slides along the boundary according to the projection of the velocity normal to the director. This applies when going back in time as well, when a trajectory first enters the domain. In this manner, every defect trajectory exists from the first frame to the final frame.

S4. FINITE-SIZE CORRECTION TO BRAIDING ENTROPY.

The E-tec topological entropy computation must be corrected for the finite size of the image domain D. This is because the trajectories that exit D are artificially fixed to the boundary, whereas the physical trajectories would engage in more braiding at the boundary of D, increasing the entropy. We estimate this extra entropy as follows. First, we distinguish between two formal dynamical systems: the full unrestricted dynamical system of the active nematic and the system restricted to the image domain D. We denote by λ_f and H_f the Lyapunov exponent and metric entropy of the full dynamical system, respectively; λ_r and H_r are the same quantities for the restricted system. We assume both systems can be modelled as uniformly hyperbolic systems. For such systems, it is known that $\lambda = H + r$, where λ and H are the Lyapunov exponent and metric entropy and r is the escape rate [48]. The full system has no escape, so $\lambda_f = H_f$. For the restricted system, we have $\lambda_r = H_r + r$. Because the Lyapunov exponent is computed as a space and time average (see Supplementary Section S5), and because the image domain D is assumed to adequately sample the statistics of the full system, we find $\lambda_r = \lambda_f$. Thus, $H_f = H_r + r$. Since the topological entropy is approximately equal to the metric entropy, we take r to be a correction to the topological entropy as well, so $h_{\mathrm{braid}} = h_{\mathrm{Etec}} + r$, where $h_{\mathrm{braid}} = h_f$ and $h_{\mathrm{Etec}} = h_r$ are the topological entropies for the full and restricted systems, respectively.

S5. COMPUTATION OF LYAPUNOV EXPONENTS.

The standard definition of the Lyapunov exponent is based on the separation rate of nearby trajectories evaluated over long time intervals. The behavior of nearby trajectories can be evaluated by the derivative of the flow map $F_{t_0}^t$, which maps an initial point r_0 in the fluid at time t_0 to the point $r(t) = F_{t_0}^t(r_0)$ at time t. Since we are interested here in (approximately) area-preserving 2D flows, we focus on the single positive Lyapunov exponent. A finite-time approximation to the Lyapunov exponent can be computed as $(\ln(\mu(r_0, t)))/t$ where $\mu(r_0, t)$ is the maximum of $||\hat{m} \cdot \nabla F_{t_0}^t||$, maximized over all unit vectors $\hat{m}$. The quantity $\mu(r_0, t)$ is also equal to the largest singular value of $\nabla F_{t_0}^t$ or one-half the largest eigenvalue of $(\nabla F_{t_0}^t)^T \nabla F_{t_0}^t$. Here we define $(\nabla F_{t_0}^t)\hat{m} = \hat{m} \cdot \nabla F_{t_0}^t$. One special property of the nematic system is that its extensile nature dictates that the direction of largest stretching $\hat{m}$ is along the nematic director $\hat{n}$, which is known from the images of the microtubules. So, we do not have to search for the maximizing vector, which significantly simplifies the Lyapunov exponent computation. Furthermore, the direction of maximum stretching $\hat{n}$ does not depend on the final time, a fact that is not true for a general flow. Thus,

$$\begin{aligned}\mu(r_0,t) &= |\hat{n}(t_0)\cdot\nabla F_{t_0}^{t}\cdot\hat{n}(t)| \\ &= |[(\nabla F_{t_0}^{t})\hat{n}(t_0)]\cdot\hat{n}(t)|.\end{aligned}\tag{2}$$

Here $\hat{n}(t)=\hat{n}(r(t),t)$ is the nematic director at position $r(t)$ and time t. Now, the finite-time Lyapunov exponent $(\ln(\mu(r_0,t)))/t$ generally depends on the initial position and on the final time. The (infinite-time) Lyapunov exponent is obtained as the limit

$$\boldsymbol{\lambda}(r_0) = \lim_{t\to\infty}\frac{1}{t}\ln(\mu(r_0,t))\tag{3}$$

$$= \lim_{t\to\infty}\frac{1}{t}\ln||\hat{n}(t_0)\cdot\nabla F_{t_0}^{t}||\tag{4}$$

$$= \lim_{t\to\infty}\frac{1}{t}\ln|\hat{n}(t_0)\cdot\nabla F_{t_0}^{t}\cdot\hat{n}(t)|.\tag{5}$$

The fact that this limit exists is guaranteed by Oseledec's Multiplicative Ergodic Theorem [49]. Furthermore, this theorem guarantees that, assuming the fluid is sufficiently well mixed (ergodic), the position dependence drops out of the Lyapunov exponent, $\boldsymbol{\lambda}(r_0)=\boldsymbol{\lambda}$. We adopt this assumption here.

Next, the map gradient satisfies the differential equation

$$\frac{d}{dt}\nabla F_{t_0}^{t}\Big|_{r_0} = \nabla v\Big|_{(t,r(t))}\nabla F_{t_0}^{t}\Big|_{r_0}.\tag{6}$$

The solution to this equation can be written formally with the time-ordered integral

$$\nabla F_{t_0}^{t_f}\Big|_{r_0} = T\exp\left[\int_{t_0}^{t_f}\nabla v\Big|_{(t,r(t))}dt\right],\tag{7}$$

which yields the following expression for the Lyapunov exponent

$$\begin{aligned}\boldsymbol{\lambda}(r_0) = &\lim_{t_f\to\infty}\frac{1}{t_f}\times \\ &\ln\left|\hat{n}(t_0)\cdot T\exp\left[\int_{t_0}^{t_f}\nabla v\Big|_{(t,r(t))}dt\right]\cdot\hat{n}(t_f)\right|.\end{aligned}\tag{8}$$

We would like to use ergodicity to replace the time integral with a spatial integral. In general, this is not possible due to the noncommuting nature of the ∇v terms. However, for this system we know that the direction of maximal expansion is $\hat{n}$. Let us thus consider the following differential equation for μ instead

$$\begin{aligned}\frac{d}{dt}\mu(r_0,t) = &\left[\left(\frac{d}{dt}\nabla F_{t_0}^{t}\right)\hat{n}(t_0)\right]\cdot\hat{n}(t)+ \\ &[(\nabla F_{t_0}^{t})\hat{n}(t_0)]\cdot\frac{d}{dt}\hat{n}(t).\end{aligned}\tag{9}$$

The second term vanishes because $(\nabla F_{t_0}^{t})\hat{n}(t_0)$ points in the direction $\hat{n}(t)$ and because $d\hat{n}(t)/dt$ points perpendicular to $\hat{n}(t)$, since $\hat{n}(t)$ has unit norm. Substituting Eq. (6) into Eq. (9) yields

$$\begin{aligned}\frac{d}{dt}\mu(r_0,t) &= \left[\left(\nabla v\Big|_{(t,r(t))}\nabla F_{t_0}^{t}\Big|_{r_0}\right)\hat{n}(t_0)\right]\cdot\hat{n}(t) \\ &= \hat{n}(t_0)\cdot\nabla F_{t_0}^{t}\Big|_{r_0}\cdot\nabla v\Big|_{(t,r(t))}\cdot\hat{n}(t) \\ &= \left(\hat{n}(t_0)\cdot\nabla F_{t_0}^{t}\Big|_{r_0}\cdot\hat{n}(t)\right)\left(\hat{n}(t)\cdot\nabla v\Big|_{(t,r(t))}\cdot\hat{n}(t)\right) \\ &= \mu(r_0,t)\left(\hat{n}(t)\cdot\nabla v\Big|_{(t,r(t))}\cdot\hat{n}(t)\right).\end{aligned}\tag{10}$$

The solution to this equation is

$$\mu(r_0, t_f) = \exp\left(\int_{t_0}^{t_f} \hat{n}(t) \cdot \nabla v\Big|_{(t,r(t))} \cdot \hat{n}(t)\, dt\right). \tag{11}$$

From Eq. (3), we thus have

$$\begin{aligned}\boldsymbol{\lambda} &= \lim_{t_f \to \infty} \frac{1}{t_f} \int_{t_0}^{t_f} \hat{n}(t) \cdot \nabla v\Big|_{(t,r(t))} \cdot \hat{n}(t)\, dt \\ &= \langle \hat{n} \cdot \nabla v \cdot \hat{n} \rangle\,, \end{aligned} \tag{12}$$

where the angled brackets represent the average over space and time. The last step follows from Birkhoff's ergodic theorem. (Actually, Birkhoff's result applies to autonomous flows and only uses the spatial average. We are making the assumption that our nonautonomous system is sufficiently statistically stationary in time that we can perform a time average.) The spatial average should be made with respect to an invariant density. We assume density variations are small enough to use the uniform density.

Our knowledge of the velocity field comes from PIV analysis of experimental movies of the microtubules. We are confident in the PIV velocity perpendicular to the director field, but not parallel to it. Thus, we are not confident in the direct computation of Eq. (12) from the tangential component of velocity. However, we can use area-preservation to recast this in terms of the perpendicular component of velocity. Local area-preservation means that the divergence of the velocity field vanishes, and thus

$$\hat{n} \cdot \nabla v \cdot \hat{n} = -\hat{n}^{\perp} \cdot \nabla v \cdot \hat{n}^{\perp}, \tag{13}$$

where $\hat{n}^{\perp}$ is the unit vector perpendicular to $\hat{n}$. We actually don't need this result to hold locally. We only need that divergence is zero on average, so that

$$\langle \hat{n} \cdot \nabla v \cdot \hat{n} \rangle = -\langle \hat{n}^{\perp} \cdot \nabla v \cdot \hat{n}^{\perp} \rangle, \tag{14}$$

where the average is over all of space and time. In summary then, we have

$$\boldsymbol{\lambda} = -\left\langle \hat{n}^{\perp} \cdot \nabla v \cdot \hat{n}^{\perp} \right\rangle. \tag{15}$$

This formula for $\boldsymbol{\lambda}$ has a simple geometric interpretation. The quantity $-\hat{n}^{\perp} \cdot \nabla v \cdot \hat{n}^{\perp}$ is the rate at which neighboring nematic contours approach one another. In general this rate varies somewhat in space and time, and hence one must average to get the overall Lyapunov exponent.

Supplementary Fig. 3 is a histogram of $-\hat{n}^{\perp} \cdot \nabla v \cdot \hat{n}^{\perp}$ for all PIV gridpoints and all frames. The black vertical line is the mean $-\langle \hat{n}^{\perp} \cdot \nabla v \cdot \hat{n}^{\perp} \rangle = 0.0120\ \mathrm{s}^{-1}$, which we take to be the Lyapunov exponent. We checked the robustness of the mean with respect to different settings for the PIV analysis in PIVlab. These gave a variation of about 5% of the mean. We use this percentage as the standard error for the value of the Lyapunov exponent computed from the PIV data.

Recent work [17, 21, 23] has also employed the PIV velocity gradient, using the Okubo-Weiss parameter $-\det(\nabla \mathbf{v})$. However, there are important differences between the Okubo-Weiss parameter and our computation of the Lyapunov exponent. Specifically, the Okubo-Weiss parameter is used to distinguish predominantly rotational motion in the lab frame (negative parameter values) from predominantly stretching behavior (positive parameter values). In contrast, when computing the Lyapunov exponent, we use only one component of the velocity gradient, the diagonal component in the direction perpendicular to the nematic director. This provides solely a measure of local stretching, and is independent of the local rotation. In our approach, a positive value of this diagonal component indicates that neighboring side-by-side microtubules are separating from each other, whereas a negative value indicates that they are being compressed together. Finally, we note that the Lyapunov exponent is fundamentally a Lagrangian concept, being computed along an advected fluid parcel, whereas the Okubo-Weiss field is fundamentally Eulerian, being referenced to the lab frame.

[48] Lai, Y.-C. & Tél, T. *Transient Chaos* (Springer, New York, NY, 2010).
[49] Young, L.-S. Mathematical theory of lyapunov exponents. *Journal of Physics A: Mathematical and Theoretical* **46**, 254001 (2013).

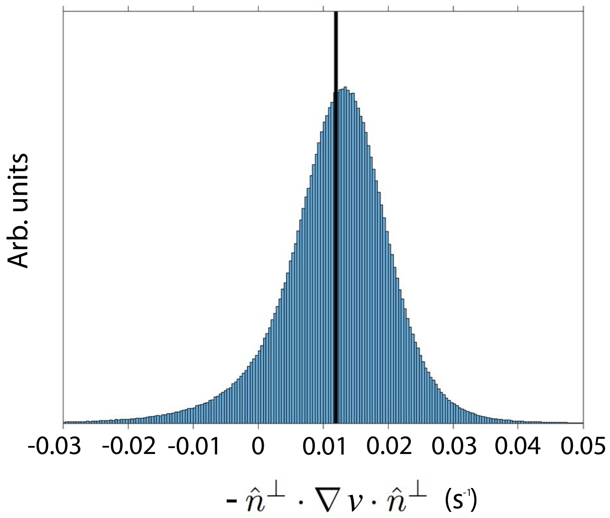

FIG. S4. The distribution of local Lyapunov exponents computed from the PIV velocity field of the fluorescence data at 50 μM ATP concentration. The vertical line is the mean 0.0120 s^{-1} of the distribution.

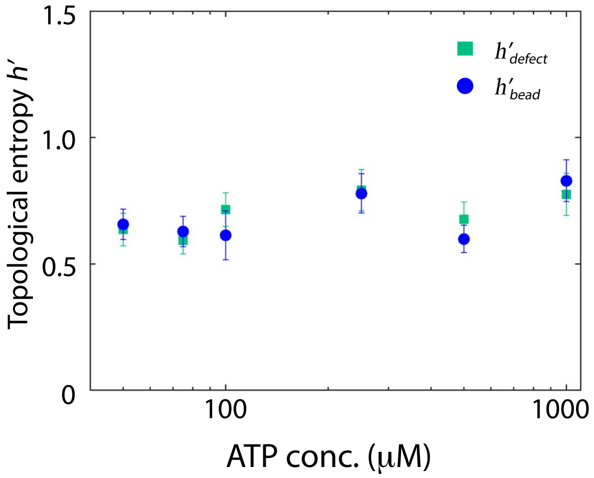

FIG. S5. Comparison of the nondimensionalized topological entropy computed from the stretching rate of nematic contours between beads (h'_{bead}) and between topological defects (h'_{defect}). Entropies are plotted as a function of varying the ATP concentration. Over the entire range of ATP concentrations, the two techniques agree within error bars.

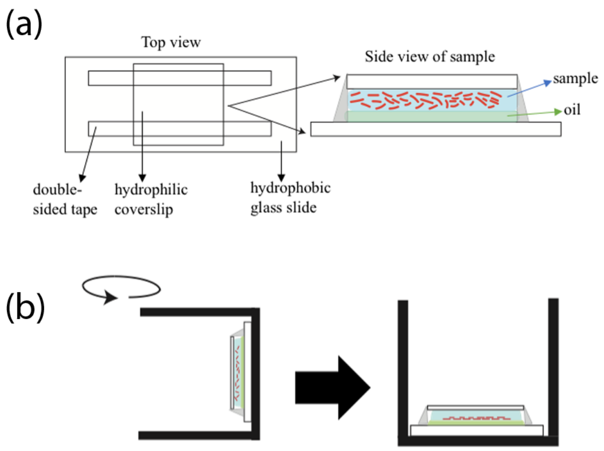

FIG. S6. Experimental setup schematics. (a) The flow cell is constructed using two strips of double-sided tape to create a channel on a hydrophobic glass slide. A pre-treated hydrophilic cover-slip is placed on top to seal the flow-cell. The aqueous protein solution sits on top of a layer of oil inside the flow cell. (b) To sediment the microtubule/kinesin bundles to the 2D oil-water interface, the flow cell is placed at the bottom of a swinging bucket rotor and centrifuged at 350 rpm for 42 min.

List of Supplementary Movies

1. Fluorescence microscope movie of the microtubule/kinesin active nematic at 50 μM ATP concentration.
2. Fluorescence microscope movie of the active nematic with topological defects tracked at 50 μM ATP concentration. +1/2 defects are shown by white circles and -1/2 defects are shown by yellow triangles.
3. Optical microscope bright field movie of the active nematic with tracked beads marked in blue and numbered. 50 μM ATP concentration.
4. Optical microscope bright field movie of the active nematic at 50 μM ATP concentration with tracked beads marked and numbered. A nematic contour growing between a pair of tracked beads is shown in blue.
5. Fluorescence microscope movie of the active nematic at 50 μM ATP concentration with topological defects marked and tracked. +1/2 defects are shown by white circles and -1/2 defects are shown by yellow triangles. A nematic contour growing between a pair of tracked defects is shown in blue.
6. Braiding motion of the tracked +1/2 defects with E-tec triangulation showing the growth of the stretched mesh (red lines). 50 μM ATP concentration.